



PII: S0749-6419(98)00003-5

ON THE GROWTH OF SHEAR BANDS AND FAILURE-MODE TRANSITION IN PRENOTCHED PLATES: A COMPARISON OF SINGLY AND DOUBLY NOTCHED SPECIMENS

M. Zhou,^{1*} A. J. Rosakis² and G. Ravichandran²

¹The George Woodruff School of Mechanical Engineering, Georgia Institute of Technology, Atlanta, GA 30332-0405, U.S.A.

²Graduate Aeronautical Laboratories, California Institute of Technology, Pasadena, CA 91125, U.S.A.

(Received in final revised form 10 November 1997)

Abstract—Recent studies of the initiation and propagation of shear bands using doubly or singly notched plates loaded asymmetrically have yielded valuable insight into this phenomenon. The same experiments also demonstrated that the shear banding mode of failure and a more brittle, “fracture”, mode of failure can coexist in the impact-loaded specimens and transitions between the two modes were documented. However, different investigators have reported significantly different types of failure mode transitions. Due to the slightly different experimental configurations used in the studies, direct comparisons could not be made to analyze the causes of the different results. This investigation focuses on isolating the cause of this discrepancy by conducting experiments on the same material using both configurations simultaneously. The results suggest that the different types of failure mode transitions are caused by the different material properties used in the studies and the difference in specimen geometry does not seem to be primarily responsible for the differing behaviors. © 1998 Published by Elsevier Science Ltd. All rights reserved

I. INTRODUCTION

The failure of structural metals under dynamic asymmetric loading has been found to take both the form of propagating shear bands and propagating cracks (Kalthoff, 1987; Kalthoff and Winkler, 1987; Mason *et al.*, 1994; Zhou *et al.*, 1996a). Because these forms of failure may often occur in real engineering materials under conditions encountered in engineering applications, understanding the intrinsic failure mechanisms involved is crucial in structural design and materials selection. The characterization of material resistance to these forms of failure could also provide guidance in the revision and improvement of engineering materials for which dynamic failure constitutes an issue.

Recently, high speed diagnostics have allowed details of the failure processes to be studied. Mason *et al.* (1994) analyzed the initiation and propagation of the shear mode of failure using the optical interferometric method of the coherent gradient sensor (CGS) and found that the deformation fields around a propagating shear band approximate the field predicted by a mode-II Dugdale model. Consequently, they obtained estimates for

*Corresponding author.

the shear stress histories inside the shear band, the stress intensity factor at band initiation as well as the time history of shear band length. Zhou *et al.* (1996a,b) studied both the shear band propagation speed histories and the temperature fields generated by the dynamically growing shear bands. The results indicated that both the band tip speed and the maximum temperature have a strong dependence on impact velocity or loading rate. In addition, finite element simulations showed that significant weakening occurs inside the band and contributes to the strong dependence of shear band tip speed on impact velocity.

Despite the insight gained through these studies, there seems to be a discrepancy in the results reported by different researchers concerning the selection of failure modes between shear banding and crack initiation in high strength steels. In studying the failure of a Ni–Co–Mo maraging steel, Kalthoff (1987) and Kalthoff and Winkler (1987) reported that at low impact velocities a crack initiates from the impact-loaded notch tips and at high impact velocities a shear band propagates from the notch tips (Fig. 1). These two forms of failure do not occur simultaneously in a specimen at any particular impact velocity. On the other hand, Mason *et al.* (1994) and Zhou *et al.* (1996a) found that at low impact velocities no failure is observed. At intermediate impact velocities a shear band initiates from the notch tip and arrests inside the specimen. In addition, a crack is observed to initiate from the tip of the arrested shear band (Fig. 2). At high impact velocities, the shear band propagates through the whole specimen and no crack is found. In the study of Kalthoff (1987) and Kalthoff and Winkler (1987), the experimental configuration involved specimens with two notches, while in the studies of Mason *et al.* (1994) and Zhou *et al.* (1996a) the specimens had one notch. Both studies used maraging steels. However, the materials may have different sets of thermal and mechanical properties as they are from separate sources.

The objective of this paper is to reconcile the difference in the results reported. The approach is to use both specimen geometries (Figs 1 and 2) and the same material for both experiments (C-300, a maraging steel, in its peak aged condition). The material is the same C-300 steel used by Mason *et al.* (1994) and Zhou *et al.* (1996a). Heat treatment of the steel involves aging at 482°C (900°F) for 4 hours followed by air cooling. The material has a hardness of 44–45 RC after the aging treatment. This approach makes it possible to make direct comparisons and to identify the factor or factors that cause the different failure transition behaviors observed in the aforementioned studies.

Figure 3 shows the geometries of the specimens used here. The single notch specimen in Fig. 3(a) is the same specimen used by Mason *et al.* (1994) and Zhou *et al.* (1996a) and the double notch specimen in Fig. 3(b) is the same configuration used by

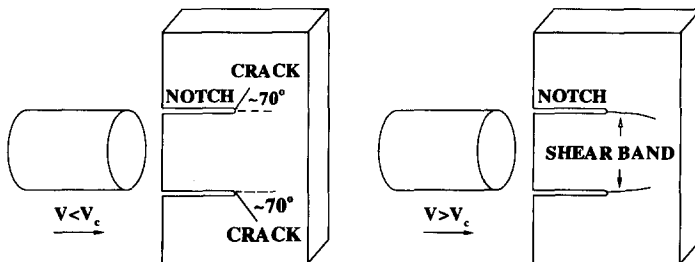


Fig. 1. Failure modes observed by Kalthoff and Winkler (1987).

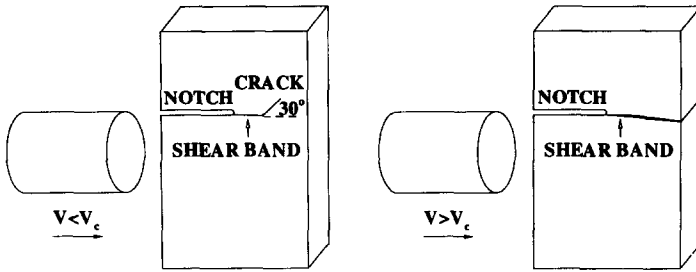


Fig. 2. Failure modes in single notch specimens.

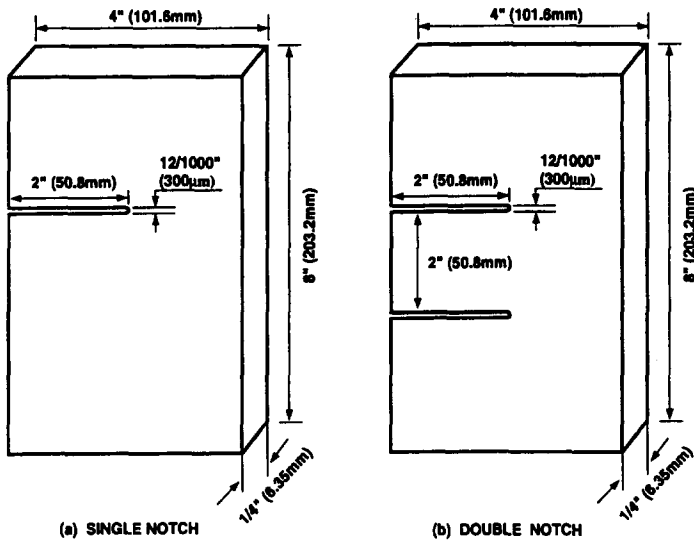


Fig. 3. Single and double notch specimens used in the current study.

Kalthoff and Winkler (1987). We focus on one representative notch size ($300\ \mu\text{m}$ in width). This is also one of the notch sizes used by Kalthoff and Winkler (1987). While the notch size may change the initiation time of failure and the critical impact velocity for failure mode transition (Kalthoff, 1987; Kalthoff and Winkler, 1987), experiments showed that it does not change the nature of the transition. Based on this finding it is reasonable to assume that the results obtained herein also apply to conditions involving a range of notch tip radii. During experiments, the specimens are impacted by a cylindrical projectile 50.8 mm in diameter and 76.2 mm in length (Figs 1 and 2). At early times after impact, a mode-II type of loading is achieved when dilatational stress waves generated by the impact arrive at the notch tip. This intense shear loading causes failure to initiate from the tip of the notch.

II. OBSERVED FAILURE MODES

The results for the single notch specimen (Fig. 3(a)) have been reported in Mason *et al.* (1994) and Zhou *et al.* (1996a) and summarized in Fig. 2. Figure 4 summarizes the failure

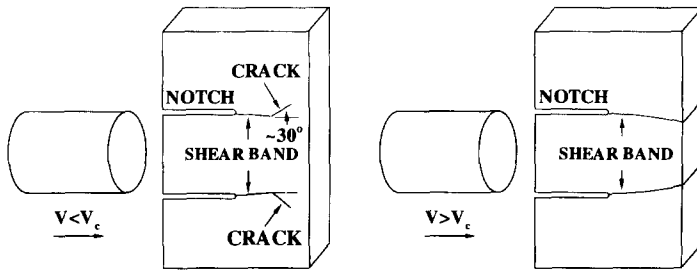


Fig. 4. Failure modes observed in double notch specimens used in the current study.

modes observed in double notch specimens of Fig. 3(b). Clearly, a very similar behavior is exhibited by both types of specimens. The similar results indicate that for the same material these two specimen geometries do not account for the difference between the failure behavior as reported by Kalthoff and Winkler (1987), Mason *et al.* (1994) and Zhou *et al.* (1996a). Indeed, the failure mode transition from shear banding to fracture observed here partly depends on evolutions of loading conditions in the specimens, (Zhou *et al.*, 1996b). The occurrence of this transition demonstrates that the material is susceptible to failure by both shear banding and by the initiation of cracks. Therefore, under dynamic conditions propagating shear bands and propagating cracks represent alternative forms of failure for the material studied.

The failure behavior observed here is in disagreement with the failure behavior reported by Kalthoff and Winkler (1987). Because both sets of experiments were conducted using the same specimen geometry and impact configuration it therefore appears that the different type of failure mode transition reported by Kalthoff (1987) and Kalthoff and Winkler (1987) is related to the fact that the high strength maraging steel used in their study has a set of properties that makes it easier for cracks to initiate from the notch tips at lower impact velocities. Indeed, material properties play an important role in determining the selection of failure modes. Zhou *et al.* (1996b) used a critical strain criterion for the initiation and propagation of shear bands and a critical stress criterion for the initiation of cracks. Calculated results obtained agree well with experimental measurements of shear band speed, temperature rise and the occurrence of failure mode transition.

III. COMPARISON OF TEMPERATURE PROFILES GENERATED BY PROPAGATING SHEAR BANDS

High speed infrared detectors are used to measure the temperature fields around the propagating shear bands during the experiments for both types of specimens shown in Fig. 3. Measurement of the temperature fields around shear bands provides more detailed comparison of shear band behaviors in these two types of specimens.

The experimental set up is that described in Zhou *et al.* (1996a). This is a non-contact measurement. The detector array used has 16 elements which collect infrared radiations from 16 square areas on the specimen, as shown in Fig. 5. Temperatures reported here are average values over these finite regions. During the experiments, the detector array is focused on a line perpendicular to the shear band, 3 or 6 mm from the tip of the notch. As the shear band propagates toward and passes through the line of observation, infrared radiations from the 16 areas along the line are collected by the detectors and the voltage

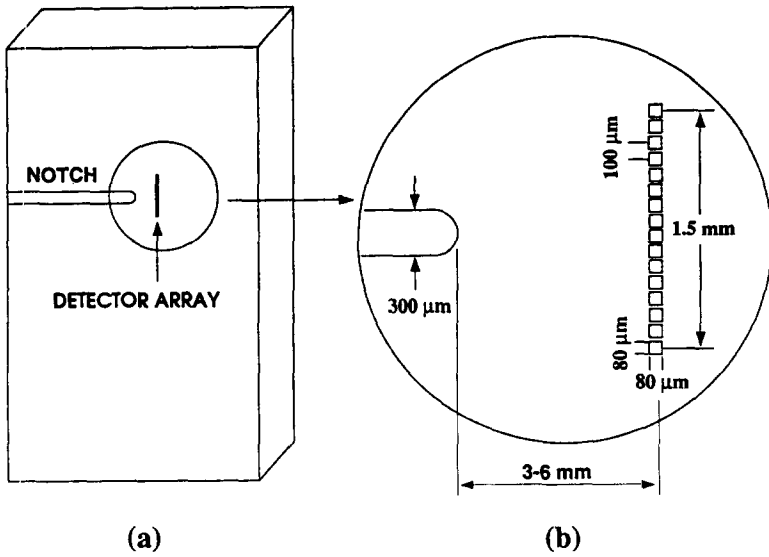


Fig. 5. A schematic illustration of the infrared.

output are recorded by high speed digital oscilloscopes. The temperature profiles around the shear bands are then obtained from the recorded detector voltage output through pre-determined detector calibration curves.

The temperature profiles measured at 3 and 6 mm from the notch tip for the single notch specimen at an impact velocity of $V_0 = 27 \text{ m s}^{-1}$ is shown in Fig. 6. The vertical axis represents temperature. The short axis in the horizontal plane represents distance along the line of measurement (direction perpendicular to the propagating band). The

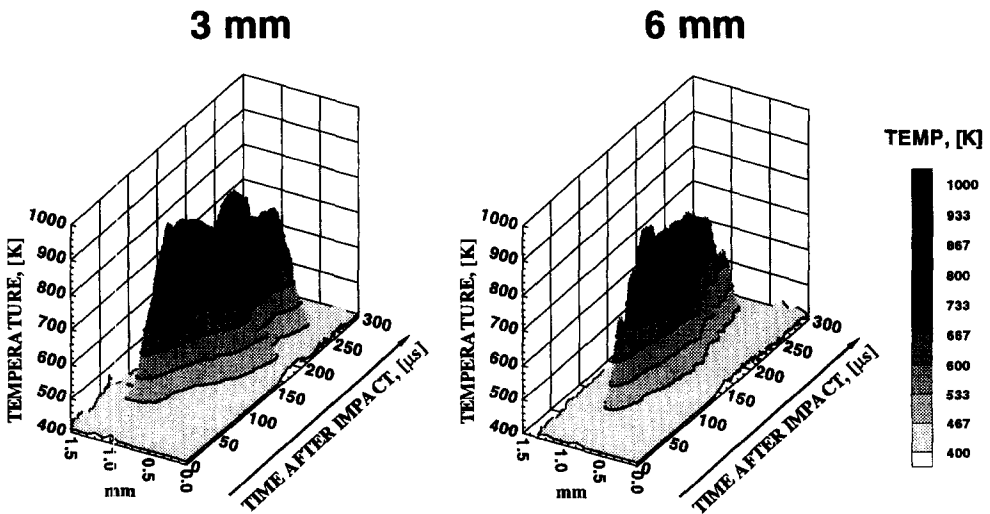


Fig. 6. Comparison of temperature profiles around propagating shear bands at 3 mm and 6 mm from notch tip, (Single notch, $V_0 = 27 \text{ m s}^{-1}$).

long axis in the horizontal plane signifies time after impact. The arrows point to the direction of increasing time. This can also be interpreted as the direction of shear band propagation. The 3-D contour plots reveal the spatial structure of the temperature fields generated by the propagating shear bands. Note that the detectors used are only sensitive to temperatures above approximately 410 K (117°C) for the C-300 steel.

The two profiles in Fig. 6 are very similar to each other in general. The maximum temperature at 3 mm (980 K) is slightly higher than that measured at 6 mm from the notch tip (930 K). Also, the profile at 3 mm is slightly wider, reflecting the larger deformation zone near the notch tip and slightly longer time for thermal diffusion there. Similar results are also obtained for the double notch specimen geometry. The lack of significant difference in these profiles indicate that the propagating shear band can be regarded as a self-similar entity over the time period and distance discussed. A detailed look at the temperature profiles reveals that the apparent two-dimensionality of the temperature fields has a length scale of approximately 400–500 μm . However, this does indicate the shear band can be treated as a one-dimensional entity for distances longer than 400–500 μm . It should be pointed out that over the entire length of the shear band there is a significant variation of temperature and deformation as the shear band propagates. In addition, since the band is not a stationary entity, temperature rises do not occur simultaneously along the band length. The time representations of temperature profiles obtained at fixed locations do not directly reflect the complete spatial distributions of temperature along the shear band. The numerical simulations of Zhou *et al.* (1996b) demonstrated that the variation of temperature along the shear band is significant and in part due to the continued deformation and heat generation behind the travelling tip.

Because of the similar results obtained over the distance of 3–6 mm from the notch tip, attention is now focused on the temperature profiles measured at 3 mm from the initial notch tip. Figure 7 compares the temperature profiles measured at this distance from the notch tip under an impact velocity of $V_0 = 27 \text{ m s}^{-1}$ for both the single and double notch specimens. The maximum temperature for the single notch specimen is slightly higher

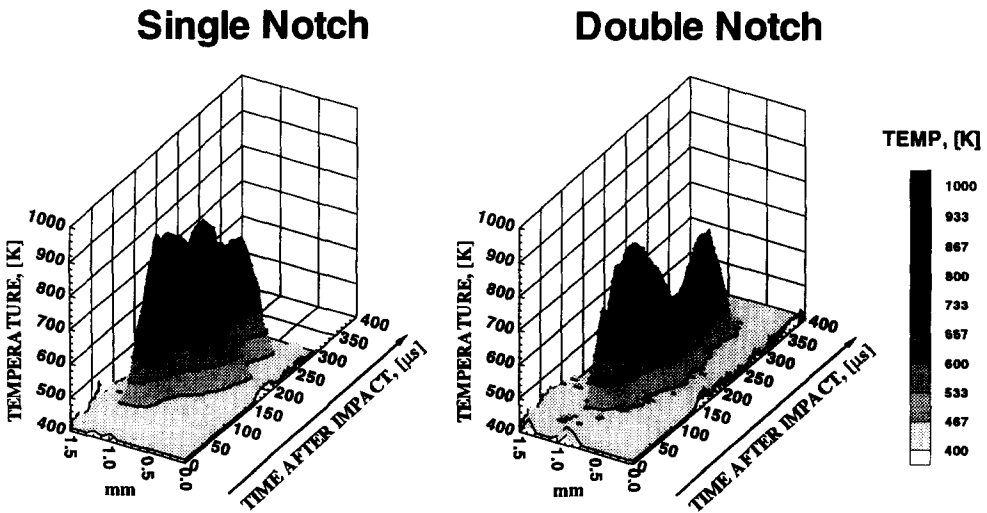


Fig. 7. Comparison of temperature profiles around propagating shear bands for single and double notch geometries (3 mm from tip, $V_0 = 27 \text{ m s}^{-1}$).

(980 K) than that for the double notch specimen (910 K). For up to $200 \mu\text{s}$ after impact, the shapes of the profiles are similar to each other, including the rise time for temperature to reach the maxima. The differences in the profiles for times after $200 \mu\text{s}$ are in consequential because that part of the record is not related to the shear band initiation, propagation and arrest. Rather, the growth of shear band occurs when a well-characterized shear loading condition exists in the specimens and this condition ceases to exist after $200 \mu\text{s}$ (Zhou *et al.*, 1996b). Overall, the profiles for the two specimen configurations are very similar, suggesting there is no significant difference in the shear band propagation behavior. This is consistent with observations of similar shear band paths in the two types of specimens after impact for the same impact velocities.

The dependence of temperature on impact velocity (or loading rate) is demonstrated in Fig. 8. The temperature profiles shown are for the double notch geometry and the detectors are focused at 3 mm from the initial notch tips. The dramatic increase in temperature with impact velocity (910 K at $V_0 = 27 \text{ m s}^{-1}$ to 1210 K at $V_0 = 40 \text{ m s}^{-1}$) is clear. This is consistent with the earlier observation of a strong dependence of temperature on impact velocity in the single notch specimen geometry (Zhou *et al.*, 1996a). Indeed, higher loading rates corresponds to higher shear band speeds and are in turn related to higher temperatures inside the bands.

The results shown in Figs 4 and 6–8 point to consistent performance by the single and double notch specimens. There is no disagreement in observed failure modes and failure mode transition. In addition, the temperature profiles and temperature levels are similar for shear bands in the two types of specimens. Furthermore, similar temperature dependence on impact velocity is observed for both specimen geometries.

IV. NUMERICAL ANALYSIS

Finite element simulations described here are based on a finite deformation formulation of Lemonds and Needleman (1986), Needleman (1989), and Needleman and Tvergaard (1991).

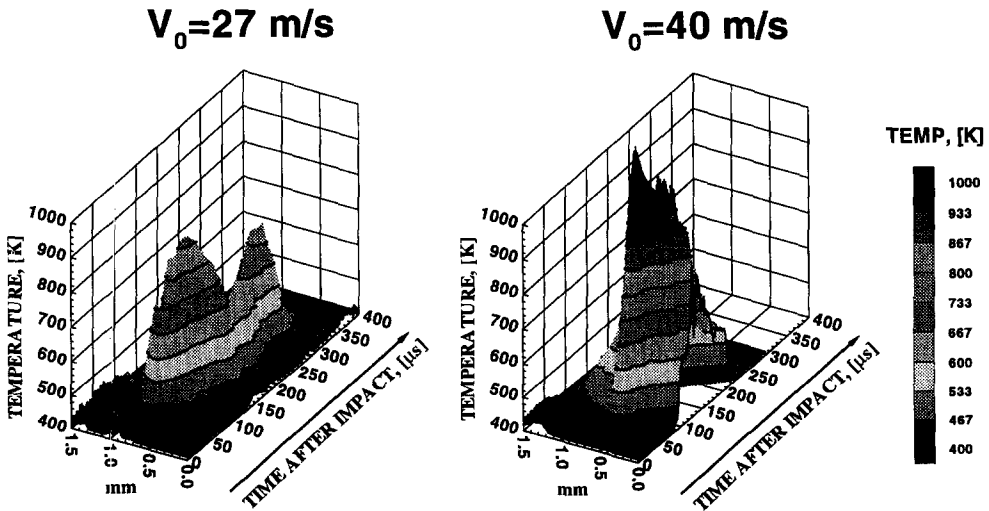


Fig. 8. Comparison of temperature profiles around propagating shear bands for different impact velocities (double notch, 3 mm from tip).

The simulation considers the full coupling between the thermal and mechanical processes of dynamic deformation.

IV.1. Governing equations

The coupled field equations are the dynamic principle of virtual work which specifies balance of momentum

$$\int_V \boldsymbol{\tau} : \delta \mathbf{D} dV = \int_S \mathbf{t} \cdot \delta \dot{\mathbf{u}} dS - \int_V \rho \frac{\partial^2 \mathbf{u}}{\partial t^2} \cdot \delta \dot{\mathbf{u}} dV, \quad (1)$$

and the variational form of heat equation which specifies balance of energy

$$\int_V \rho c_p \dot{T} \delta T dV = \int_V \chi \boldsymbol{\tau} : \mathbf{D}^p \delta T dV + \int_S k(\mathbf{F}^{-1} \mathbf{F}^{-T} \nabla T) \cdot \mathbf{N} \delta T dS - \int_V k(\mathbf{F}^{-1} \mathbf{F}^{-T} \nabla T) \cdot \nabla \delta T dV. \quad (2)$$

In the above equations, V and S represent, respectively, the volume and surface of a body in the reference configuration, $\boldsymbol{\tau} = J\boldsymbol{\sigma} = \det |\mathbf{F}| \boldsymbol{\sigma}$ is the Kirchhoff stress, with $\boldsymbol{\sigma}$ the Cauchy stress, and \mathbf{F} is the deformation gradient. \mathbf{t} is the traction on a surface with normal \mathbf{N} in the reference configuration, \mathbf{u} is the displacement, \mathbf{D} denotes the rate of deformation, t is time, ρ is mass density in the reference configuration, T is temperature, χ denotes the fraction of plastic work converted to heat, \mathbf{D}^p is the plastic part of the rate of deformation, c_p is specific heat, k is heat conductivity, χ is the fraction of plastic work converted to heat, (\cdot) denotes $\partial/\partial t$, $\mathbf{A}:\mathbf{B}$ is $A^i B_{ji}$, ∇ denotes gradient in the reference configuration, $(\cdot)^{-1}$ and $(\cdot)^{-T}$ denote, respectively, inverse and inverse transpose, δT , $\delta \mathbf{D}$ and $\delta \dot{\mathbf{u}}$ denote admissible variations in temperature, rate of deformation and velocity, respectively.

IV.2. Constitutive relations

The constitutive relation is written as (Povirk *et al.*, 1993),

$$\hat{\boldsymbol{\tau}} = \mathbf{L} : [\mathbf{D} - \mathbf{D}^p - \alpha \dot{T} \mathbf{I}], \quad (3)$$

where $\hat{\boldsymbol{\tau}}$ the Jaumann rate of Kirchhoff stress, \mathbf{L} is the tensor of elastic moduli, α is the coefficient of thermal expansion, and \mathbf{I} is the second order identity tensor. For an isotropically hardening, viscoplastic solid $\mathbf{D}^p = \frac{3\dot{\bar{\epsilon}}}{2\bar{\sigma}} \boldsymbol{\tau}'$, with $\dot{\bar{\epsilon}}$ being the equivalent plastic strain rate, $\boldsymbol{\tau}' = \boldsymbol{\tau} - \frac{1}{3}(\boldsymbol{\tau} \cdot \mathbf{I})\mathbf{I}$ and $\bar{\sigma}^2 = \frac{3}{2} \boldsymbol{\tau}' \cdot \boldsymbol{\tau}'$.

The viscoplastic response of the material for the strain rate range of 10^{-3} s^{-1} to $1.5 \times 10^3 \text{ s}^{-1}$ is measured experimentally using quasistatic compression and split Hopkinson compression bar, as reported by Mason *et al.* (1994). The measured stress-strain curves are shown in Fig. 9 and are used to obtain a viscoplastic model characterization which involves the following equations.

$$\left. \begin{aligned} \dot{\bar{\epsilon}} &= \dot{\epsilon}_0 \left[\frac{\bar{\sigma}}{g(\bar{\epsilon}, T)} \right]^m, \\ g(\bar{\epsilon}, T) &= \sigma_0 (1 + \bar{\epsilon}/\epsilon_0)^n \left\{ 1 - \Delta \left[\exp \left(-\frac{T - T_0}{K} \right) - 1 \right] \right\}, \end{aligned} \right\} \quad (4)$$

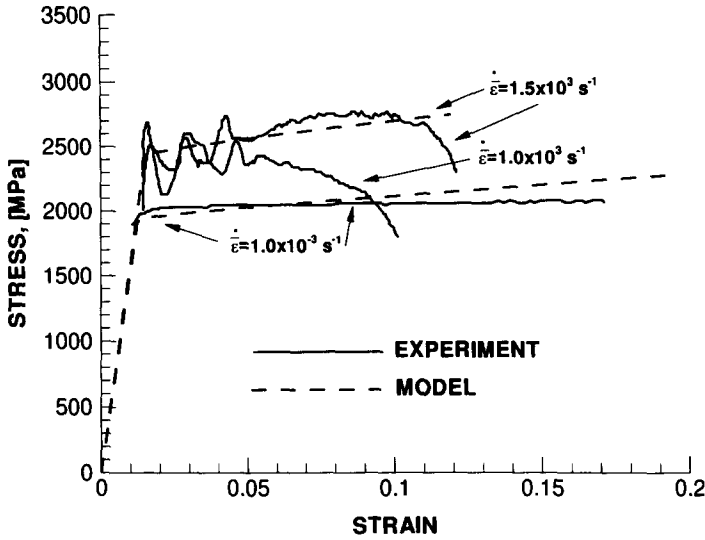


Fig. 9. Stress-strain curves for C-300 steel.

where $\bar{\epsilon} = \int_0^t \dot{\epsilon} dt$ is the equivalent plastic strain, $\dot{\epsilon}_0$ is a reference strain rate, m is a rate sensitivity parameter, σ_0 is the yield stress, $\epsilon_0 = \sigma_0/E$ is a reference strain, n is the strain hardening exponent, T_0 is a reference temperature, and Δ and κ are thermal softening parameters. The function $g(\bar{\epsilon}, T)$ represents the stress-strain relation at the quasi-static strain rate of $\dot{\epsilon}_0$ and at temperature T . At $T = T_0$, $g(\bar{\epsilon}, T) = \sigma_0(1 + \bar{\epsilon}/\epsilon_0)^n$. Most of these constitutive law parameters are determined by fitting the measured curves. The fitted curves are shown in Fig. 9 along with the measured curves. Note that the curves are plotted using the equivalent stress and the total equivalent strain here whereas in Mason *et al.* (1994) the same curves are plotted using shear stress and shear strain. Values of the parameters used in the simulations are listed in Table 1.

IV.3. Failure criteria

In addition to thermal softening, localized deformations are also accompanied by material weakening due to the formation of microvoids. The extensive damage and failure through void initiation, growth and coalescence observed inside the shear bands in experiments (Zhou *et al.*, 1996a) attest to the important role of such weakening mechanisms in the initiation and propagation of shear bands in this material. In the present paper, the process of void development is not explicitly simulated. Rather, the material weakening is modelled by the use of a failure criterion and a constitutive characterization that specifies lower stress-carrying capabilities for damaged materials. Specifically, ductile failure is assumed to initiate when the equivalent plastic strain reaches a certain critical value. The failure condition is given by

$$\bar{\epsilon}_c = \epsilon_1 + (\epsilon_2 - \epsilon_1) \frac{\dot{\epsilon}_r}{(\dot{\epsilon}_r + \bar{\epsilon})}, \quad (5)$$

Table 1. Material parameters for C-300 steel

Parameter	Value
$\dot{\epsilon}_0$	$1 \times 10^{-3} \text{s}^{-1}$
m	70
σ_0	2000 MPa
ϵ_0	σ_0/E
n	0.01
T_0	293 K
Δ	0.8
κ	500 K
E	200 GPa
ν	0.3
ρ	7830 kgm^{-3}
c_p	$448 \text{ J}(\text{kg K})^{-1}$
k	$34.6 \text{ W}(\text{m K})^{-1}$
α	$11.2 \times 10^{-6} \text{ K}^{-1}$
χ	0.9

where ϵ_1 and ϵ_2 are, respectively, the critical strains at which the material is assumed to lose significantly its stress-carrying capability as $\dot{\epsilon} \rightarrow \infty$ and at $\dot{\epsilon} = \dot{\epsilon}_0$. Also, $\dot{\epsilon}_r$ is a rate-dependence parameter. The motivation to choose such a rate-dependent form for the critical strain is the experimental observation that at higher strain rates materials localize and fail at lower levels of plastic strains. Such a simple criterion may not capture all the complicated features of the failure occurring inside the shear bands. Rather, it is a phenomenological characterization that allows the initiation and propagation of shear bands to be studied under a relatively simple theoretical framework. Once the critical strain $\bar{\epsilon}_c$ is reached (eqn (5)), the damaged material is modelled to behave like a viscous fluid. Specifically, the stress-carrying capability by the material is assumed to follow that of a Newtonian fluid, carrying both a hydrostatic pressure component and a viscous stress component, i.e.

$$\boldsymbol{\tau} = -\frac{\gamma[1 - J + \alpha(T - T_0)]}{j} \frac{E}{1 - \nu} \mathbf{I} + \mu \mathbf{D}, \quad (6)$$

where γ is a stiffness parameter and μ is the viscosity. The use of such a constitutive relation for materials inside the shear band is motivated by their ability to sustain pressure, by the continued dissipation through deformation and frictional forces and by the high temperature values observed in the experiments.

The above critical strain criterion is appropriate in describing shear-dominated ductile failure. In order to account for the possibility of other mechanisms of material decohesion, tensile failure, we introduce the following additional failure condition. Tensile failure is assumed to occur when the maximum tensile stress exceeds a certain value, or

$$\sigma_{\max} \geq \sigma_{\text{cr}}, \quad (7)$$

where σ_{cr} is a crucial threshold stress for failure. It is taken to be equal to 3 times the yield stress to account for the effect of high triaxiality which is expected to dominate at the tip

Table 2. Damage model parameters

Parameter	Value
ϵ_1	$4\sigma_0/E$
ϵ_2	0.3
ϵ_r	$4 \times 10^4 \text{s}^{-1}$
γ	0.002
μ	$5 \times 10^{-4} \text{MPa}\cdot\text{s}$
σ_{cr}	$3\sigma_0$

of an initiating crack in a ductile solid. The material is assumed to have no tensile stress-carrying capability after either criterion (eqns (5) and (7)) is satisfied. Specifically in the analysis, the hydrostatic component of the stress is non-positive or $\tau:\mathbf{I} \leq 0$ for failed material elements. The relevant material parameters in eqns (5)–(7) appear in Table 2.

The use of the above failure criteria allows the initiation and propagation of shear bands and the evolution and transition of failure modes to be simulated. Also, the effects of various factors, such as impact velocity and different combinations of material properties, can be explored.

IV.4. Finite element method

When the finite element approximations of the displacement and temperature fields are substituted into the momentum balance eqn (1) and the energy balance eqn (2), the resulting equations take the forms,

$$\mathbf{M} \frac{\partial^2 \mathbf{U}}{\partial t^2} = \mathbf{R}, \quad (8)$$

and

$$\mathbf{C} \frac{\partial \mathbf{T}}{\partial t} = -\mathbf{K}\mathbf{T} + \mathbf{H}, \quad (9)$$

where \mathbf{U} is the vector of nodal displacements, \mathbf{T} is the vector of nodal temperatures, \mathbf{M} , \mathbf{C} and \mathbf{K} are the mass, the heat capacitance and the heat conductance matrices, and \mathbf{R} and \mathbf{H} are the mechanical and thermal force vectors, respectively.

A lumped mass matrix is used in eqn (7), for reasons of efficiency and accuracy, (Krieg and Key, 1973). Equation (7) is integrated using the Newmark β -method, with $\beta = 0$ and $\gamma = 0.5$ (Belytschko *et al.*, 1976). The integration of eqn (8) using a lumped heat capacitance matrix and the numerical scheme for solving the coupled system of eqns (8) and (9) are discussed in Zhou *et al.* (1994).

In the calculations, the specimens shown in Fig. 3 are initially at rest and stress-free. The boundary conditions are such that the surfaces are traction-free throughout the deformation except where the specimens come into contact with the projectile. For the single-notch specimen, this area is on the lower side of the notch and has a width of 50.8 mm. For the double-notch specimen, the contact zone is between the two notches.

Only one half of the double notch specimen is used in the actual calculations because of symmetry with respect to the x -axis. A velocity boundary condition is applied in the contact zones for both specimens. The applied velocity is equal to the impact velocity and is in the direction of projectile motion.

The objective of the analysis is to compare the deformation conditions for these two specimen geometries and identify their influence on the initiation and propagation of shear bands and failure mode transition in the experiments. Since the numerical results for the single notch case have been reported in Zhou *et al.* 1996b), attention is now focused on the double notch geometry. Comparisons are also made between the two sets of results.

Figure 10 compares the histories of the generalized path-independent J -integral for dynamic conditions (Nakamura *et al.*, 1985; Moran and Shih, 1987a,b) in these two specimens under an impact velocity of 25 m s^{-1} . This J -integral is given by

$$J = \int_{\Gamma} \left[\left(\int_0^t \boldsymbol{\tau} : \mathbf{D} dt - \int_{T_0}^T \boldsymbol{\tau} : \mathbf{I} dT + \frac{1}{2} \rho \dot{\mathbf{u}} \cdot \dot{\mathbf{u}} \right) dx_2 - \mathbf{t} \cdot \frac{\partial \mathbf{u}}{\partial x_1} ds \right] + \int_A \left[\alpha(\boldsymbol{\tau} : \mathbf{I}) \frac{\partial T}{\partial x_1} + \rho \dot{\mathbf{u}} \cdot \frac{\partial \mathbf{u}}{\partial x_1} - \rho \dot{\mathbf{u}} \cdot \frac{\partial \dot{\mathbf{u}}}{\partial x_1} \right] dA, \quad (10)$$

where A is the area inside contour Γ , x_1 and x_2 are Cartesian coordinates in the reference configuration. A series of 10 contours of different sizes emanating from the notch surfaces are used in the analysis. As expected, the calculated J values for these contours remain the same until they are intercepted by the shear band tip. This interception corresponds to the time when a failure criterion is met at a point on a contour intercepted by the shear band path. The values after interception are not used in the current analysis.

The J values calculated for two contours, close to but successively farther away from a notch tip, are plotted for each specimen configuration. These two J values obtained for the two contours are the same in each specimen for up to the time of shear band initiation. The initiation of shear bands (points A and B) is defined to be at the time when the first contour is intersected by the travelling tip of the shear band. After the initiation, J values calculated for the two successive contours differ and path-independence no longer holds for the contour that has been intersected by the shear band. Initially, the loading conditions around the notch tips are identical in these two types of specimens as indicated by the same J values for up to $12 \mu\text{s}$ (point A) after impact. This is because for each notch the stress waves from the projectile edge (single notch specimen) or the other notch (double notch specimen) do not arrive until this time (Figs 1–3). After the arrival of such waves, the J value for the double notch specimen is lower than that for the single notch case, indicating that the driving force for shear banding is lower when two notches are present (interaction between two notch tips). Although shear band initiation occurs at a later time in the double notch case, the critical J value at which initiation occurs (J_{init}) is very similar to that for the single geometry. This level is approximately 115 KJ m^{-3} . Previous calculations (Zhou *et al.*, 1996b) showed a dependence of J_{init} on impact velocity (or loading rate) which accounts for the slight difference since loading rates ($\dot{J}(t)$) at initiation is also different between specimen geometries. The results in Fig. 10 lends support to the idea that J may be an indicator of the driving force needed to cause a shear band to initiate or a measure of a material's resistance to the initiation and growth of shear bands.

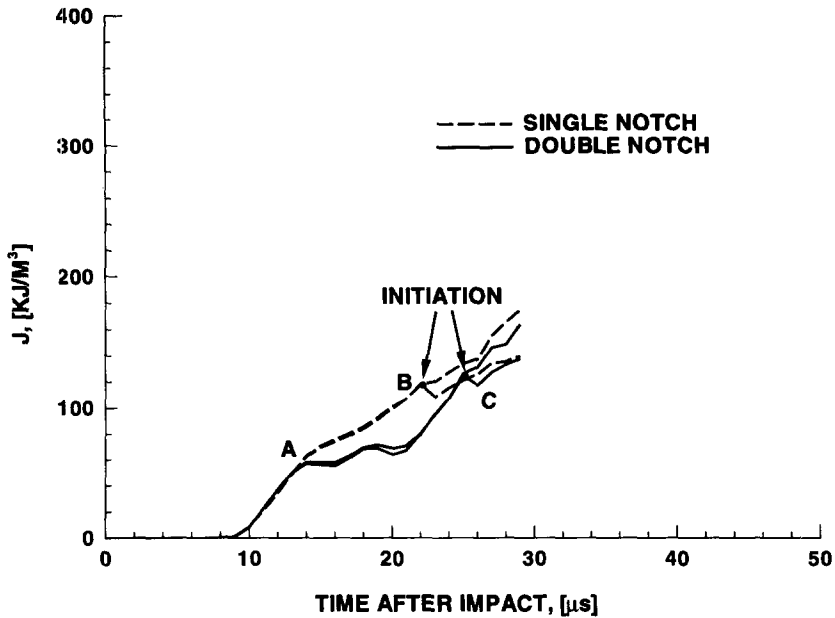


Fig. 10. Comparison of J -integral histories ($V_0 = 25 \text{ m s}^{-1}$).

The histories of the shear band length for the two specimen geometries are shown in Fig. 11. The length of the shear bands is the distance between the initial notch tip and the current tip of the band. The current tip is defined as being at the point where the ductile damage criterion of eqn (5) is first satisfied. The initiation occurs later in the double notch case due to its lower J value compared with the single notch case. This plot also indicates that the overall shear band speed is slightly lower due to stress wave interactions between the two notches. As a result of the lower speed, the total length of the band is shorter compared with that for the single notch specimen. The lower shear band length and shear band speed are consistent with the measured temperature levels inside shear bands shown in Fig. 7 for these two specimen geometries. Higher shear band speeds correspond to higher temperatures inside shear bands. For the same impact velocity of 27 m s^{-1} , the shear band in the double notch specimen has a maximum temperature (910 K) that is lower than that for the shear band in the single notch specimen (980 K) apparently because its propagating speed is lower.

Figure 12 is a comparison of the distributions of the in-plane shear stress component (σ_{12}) of the Cauchy stress tensor in the part of the specimens that is in front of the notch tip. In the single notch case of Fig. 3(a), the whole specimen is used in the calculation. In the double notch case of Fig. 3(b), only one half of the specimen is used because of symmetry. The impact occurs on the lower side of the notch as indicated in Fig. 12. The distributions of σ_{12} at two times after impact (30 and 40 μs) are shown for the each geometry. Overall, the deformation conditions in the two specimens are very similar to each other as demonstrated by the contours. A small difference develops in the intensity of the shear loading at the later time. This difference is reflected in the slightly smaller size of the area in Fig. 12(d) that has high σ_{12} values, compared with Fig. 12(c). This lower intensity of

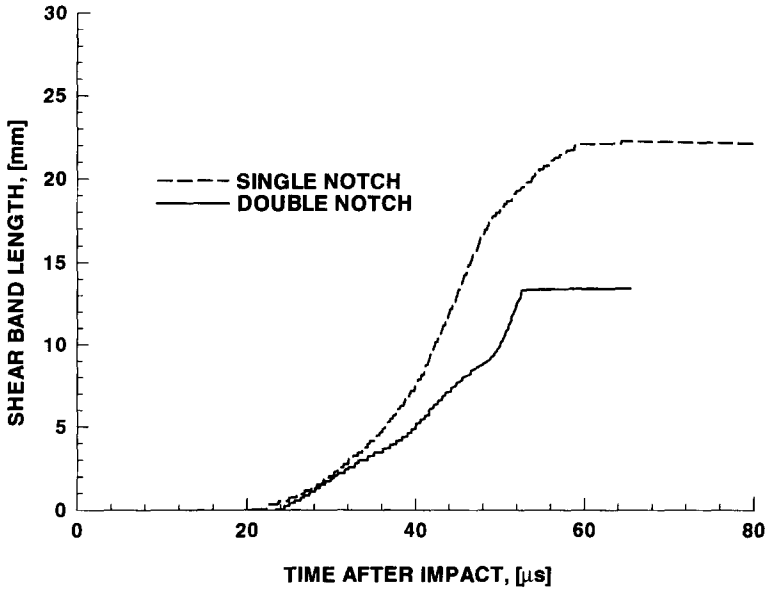


Fig. 11. Comparison of shear band length histories ($V_0 = 25 \text{ m s}^{-1}$).

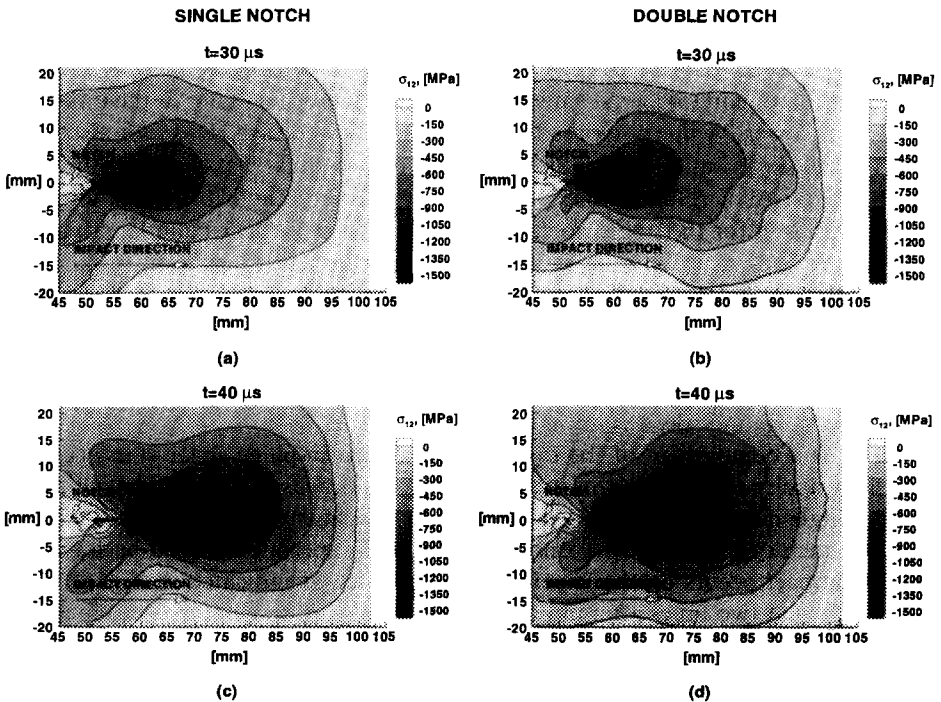


Fig. 12. Comparison of σ_{12} distributions ($V_0 = 25 \text{ m s}^{-1}$).

shear loading causes shear band to propagate slightly more slowly as seen in Fig. 11. The lower J values for double notch specimen in Fig. 10 is one measure of this lower driving force for localization.

Figure 13 compares the calculated temperature profiles and the corresponding profiles measured in experiments for the two types of specimens. The profiles correspond to temperature histories in the middle of shear bands. They are obtained by focusing a detector at a point 3 mm in front of the notch tip before impact. Details of this scheme can be seen in Fig. 5. During the deformation the shear band tip propagates toward and passes through the point of observation. The temperature profiles discussed here are the temperature histories recorded by this detector. After release waves arrive from specimen boundaries, the overall motions of the two types of specimens may be significantly different. Consequently, the areas probed by this detector in the two geometries may not represent the same relative location along the shear bands. Because of this limitation, only temperature histories for the time period of up to $60 \mu\text{s}$ after impact are shown in Fig. 13. It is clear from Fig. 11 that this time period contains the entire process of shear band initiation, propagation and arrest in both specimen geometries. Therefore the data shown are sufficient for the purpose of comparing the temperature rises inside propagating shear bands in these two types of specimens. The results shown are for an impact velocity of 25 m s^{-1} . There is a good agreement between the experimental and the calculated curves. Both the experiments and the calculations show that temperature increases slightly more slowly in the double notch specimen than in the single notch case. This is consistent with the lower shear band speed and length seen in Fig. 11. Temperatures lower than 400 K are

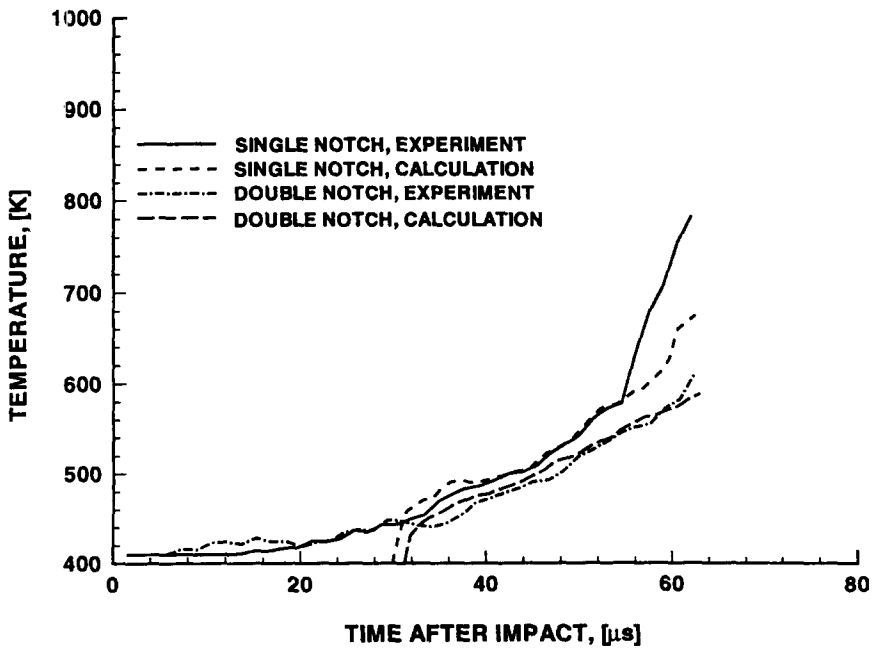


Fig. 13. Comparison of temperature increases for a point 3 mm from the notch tip, at the center of the shear band ($V_0 = 25 \text{ m s}^{-1}$).

not compared in this figure because the detectors used are only sensitive to temperatures over 410 K for the material studied. The simulations, however, capture the full range of increase from room temperature (293 K).

V. SUMMARY

The initiation and propagation of dynamic shear bands are studied experimentally using plates with both one and two pre-machined notches. For comparison purposes, the same material and notch size are used for all experiments. Along with previous results of this investigation, the experiments demonstrated that the general failure behavior and the propagation history of shear bands are consistent between these two specimen geometries. This result is in disagreement with the failure transition reported by Kalthoff and Winkler (1987). The different results obtained in the separate studies suggest that material properties play the important role in determining the selection of failure modes. The form of failure mode transition reported by Kalthoff and Winkler (1987) is likely to have been caused by the different material properties of the steel used in their investigations. Further analysis is needed in order to quantify how failure selection occurs in different materials when different properties are involved. A critical strain criterion is used for the initiation and propagation of shear bands and a critical stress criterion is used for the initiation of cracks in this and previous analyses. Calculated results agree reasonably well with experimental measurements of shear band speed, temperature rise and the occurrence of the failure mode transition observed in our experiments.

Experimental measurements of the temperature fields generated by propagating shear bands showed that the apparent length scale for the two-dimensionality of propagating shear bands in C-300 steel is approximately 400–500 μm . Measurements obtained at 3 and 6 mm from notch tips (shear band initiation sites) for both specimen geometries demonstrated that temperature profiles are very similar over such distances of shear band propagation, indicating the self-similar nature of the shear bands as they propagate. This similarity does not mean that a one-dimensional approximation applies to the temperature and deformation fields over the whole length of propagating shear bands due to the fact that temperature rises and deformation are not simultaneous along the band length.

The measurements also showed that the temperature increase for a shear band in the double notch geometry is slightly lower than that for the shear band in the single notch geometry impacted at the same projectile velocity. Finite element simulations identified the reason to be a lower driving force for localization due to stress wave interactions between notches in the double notch geometry. As a result of the lower driving force, the average shear band speed and overall shear band length are slightly lower than those in the single notch geometry.

Finite element simulations using the two specimen geometries also demonstrated that the values of J integral at the initiation of shear band are very similar for the two types of specimens.

Acknowledgements—The authors gratefully acknowledge support from the Army Research Office through grant No. DAAH 04-93-G0037 under Dr K. Iyer. We are also grateful to Dr Y. Rajapakse for support from the Office of Naval Research through grant No. N00014-90-J-1340. The computations were carried out on a Cray C98 computer at the Goddard Space Center and a Cray Y-MP2E/232 computer at the Jet Propulsion Laboratory.

REFERENCES

- Belytschko, T., Chiapetta, R. L. and Bartel, H. D. (1976) Efficient large scale non-linear transient analysis by finite elements. *Int. J. Numer. Meth. Engng.* **10**, 579–596.
- Kalthoff, J. F. and Winkler, S. (1987) Failure mode transition at high rates of shear loading. In *Impact Loading and Dynamic Behavior of Materials*, eds. C. Y. Chiem, H.-D. Kunze and L. W. Meyer, Vol. 1, pp. 185–195.
- Kalthoff, J. F. (1987) Shadow optical analysis of dynamic shear fracture. *SPIE, Vol. 1 814, Photomechanics and Speckle Metrology*, pp. 531–538.
- Krieg, R. D. and Key, S. W. (1973) Transient shell response by numerical time integration. *Int. J. Numer. Meth. Engng* **7**, 273–286.
- Lemonds, J. and Needleman, A. (1986) Finite element analyses of shear localization in rate and temperature dependent. *Solids, Mech. Mat.* **5**, 339–361.
- Mason, J. J., Rosakis, A. J. and Ravichandran, G. (1994) Full field measurements of the dynamic deformation field around a growing adiabatic shear band at the tip of a dynamically loaded crack or notch. *J. Mech. Phys. Solids* **42**(11), 1679–1697.
- Moran, B. and Shih, C. F. (1987a) Crack tip and associated domain integrals from momentum and energy balance. *Engng. Fract. Mech.* **27**, pp. 615–642.
- Moran, B. and Shih, C. F. (1987b) A general treatment of crack tip contour integrals. *Int. J. Fract.*, **35**, 295–310.
- Nakamura, T., Shih, C. F. and Freund, L. B. (1985) Computational methods based on an energy integral in dynamic fracture. *Int. J. Fract.* **27**, 229–243.
- Needleman, A. (1989) Dynamic shear band development in plane strain. *J. Appl. Mech.* **56**, 1–9.
- Needleman, A. and Tvergaard, V. (1991) An analysis of dynamic, ductile crack growth in a double edge cracked specimen. *Int. J. Frac.* **49**, 41–67.
- Zhou, M., Needleman, A. and Clifton, R. J. (1994) Finite element simulations of dynamic shear localization in plate impact. *J. Mech. Phys. Solids* **42**(3), 423–458.
- Zhou, M., Rosakis, A. J. and Ravichandran, G. (1996a) Dynamically propagating shear bands in prenotched plates: I—Experimental investigations of temperature signatures and propagation speed. *J. Mech. Phys. Solids*, **44**, 981–1006.
- Zhou, M., Ravichandran, G. and Rosakis, A. J. (1996b) Dynamically propagating shear bands in prenotched plates: ii—Finite element simulations. *J. Mech. Phys. Solids*, **44**, 1007–1032.